Automated Laser-Assisted Single-Cell Sorting for Cell Functional and RNA Sequencing

Yuntong Wang[a,b,c,d], Ying Xue[e], Huan Wang[a,b], Yue Qu[e,f], Kunlong Zhang[e], Lindong Shang[a,b,c,d], Peng Liang[a,b,c,d], Fuyuan Chen[a,b,c,d], Xusheng Tang[a,b,c,d], Wei Luo[g*], Lip Ket Chin[h*], Shilun Feng[i*], Bei Li[a,b,c,d,*]

[a] Changchun Institute of Optics, Fine Mechanics and Physics, Chinese Academy of Sciences, Changchun 130033, P. R. China

[b] University of Chinese Academy of Sciences, Beijing 100049, P. R. China

[c] State Key Laboratory of Applied Optics, Changchun 130033, P. R. China

[d] Key Laboratory of Advanced Manufacturing for Optical Systems, Chinese Academy of Sciences, Changchun 130033, P. R. China

[e] Hooke Laboratory, Changchun 130033, P. R. China

[f] Haining high-tech research institute, Jiaxing, Zhejiang, 314408, P. R. China

[g] Department of Electrical and Electronic Engineering, The Hong Kong Polytechnic University, 999077, Hong Kong SAR

[h] Department of Electrical Engineering, City University of Hong Kong, 999077, Hong Kong SAR

[I] State Key Laboratory of Transducer Technology, Shanghai Institute of Microsystem and Information Technology, Chinese Academy of Sciences, Shanghai, 200050, China

KEYWORDS: Single-cell sorting, Single-cell analysis, Laser-induced forward transfer, Micropores, RNA sequencing.

ABSTRACT: Accurate and efficient sorting of single target cells is crucial for downstream single-cell analysis, such as RNA sequencing, to uncover cellular heterogeneity and functional characteristics. However, conventional single-cell sorting techniques, such as manual micromanipulation or fluorescence-activated cell sorting, do not match current demands and are limited by low throughput, low sorting efficiency and precision, or limited cell viability. Here, we report an automated, highly efficient single-cell sorter, integrating laser-induced forward transfer (LIFT) with a high-throughput picoliter micropore array. The micropore array was surface-functionalized to manipulate liquid surface tension, facilitating the formation of single-cell picoliter droplets in the micropores to realize automated and highly efficient (>80%) single-cell isolation. Using an in-house built microscopic system, rare target cells were identified and automatically retrieved by LIFT with precise sorting efficiency (about 100%) for downstream single-cell analysis while maintaining high cell viability (about 80%). As a case demonstration, we demonstrated the accurate sorting of rare transfected PC-9 cells and post-transfection cell culture, minimizing cell loss and the risk of contamination. Furthermore, we performed single-cell RNA sequencing and showed that high-quality single-cell transcriptome information was efficiently and reliably obtained during cell sorting, preventing additional costs due to low sorting accuracy. The single-cell sorter will become invaluable for single-cell analysis, laying the foundation for multi-omics analysis and precision medicine research.

Single-cell analysis is a cornerstone of modern biological and medical research, offering unprecedented insights into cellular diversity and function.[1, 2] For instance, understanding the heterogeneity among tumor cells in cancer research is crucial for developing targeted therapies and improving patient outcomes.[3] However, existing single-cell sorting techniques often face limitations in efficiency, precision, cell viability and cost, impeding their widespread application in detailed cellular studies. Conventional methods include manual micromanipulation,[4] fluorescence-activated cell sorting (FACS)[5] and microfluidics-based techniques[6]. Manual micromanipulation provides gentle cell handling but typically yields lower efficiency and limits the number of single cells that can be analyzed.[7] FACS is still widely used because it offers high throughput and specificity but often reduces cell viability due to mechanical stress. Innovative approaches, such as droplet microfluidics, offer automated high-throughput single-cell sorting. However, most analyzed droplets are empty, which hinders efficient cell analysis and increases costs.[8] In addition, droplet microfluidics impose difficulties in downstream cell culture, which is limited by efficient cell release from the emulsion state, leading to cell loss.[9] Other microfluidic-based techniques, though precise, often face susceptibility to clogging and are limited by low throughput and technical complexity, hindering their practical application in routine single-cell analysis.[10] These challenges underscore the need for a more efficient

automated approach to single-cell sorting that is capable of (a) high-throughput single-cell isolation, (b) precise target cell identification and sorting, and (c) high cell viability to facilitate downstream culture and analysis.

Here, we demonstrate a highly efficient, automated single-cell sorter that leverages laser-induced forward transfer (LIFT) with micropore array chip technology. The surface-functionalized micropore array chip has hundreds of thousands of picoliter micropores to achieve high-throughput single-cell isolation by manipulating the surface tension of the cell-suspending sample liquid on the chip. Subsequently, an in-house optical microscopic system is employed to identify rare target cells from the heterogeneous cell population and sort target cells via the LIFT mechanism with high efficiency. The micropore array-based single-cell sorter maintains the cell viability of target cells, enabling downstream single-cell culture and analysis. We demonstrate its ability to accurately sort and culture target cells from transfected cell lines. In addition, we perform single-cell RNA sequencing, facilitating comprehensive genetic profiling of individual cells and preventing additional costs associated with low sorting accuracy and cell viability. The micropore array-based laser-assisted single-cell sorter has the potential to revolutionize single-cell studies and significantly impact cancer research and beyond in genetic and functional studies.

METHODS

Optical Microscopic System. The laser-assisted single-cell sorter (PRECI SCS, HOOKE Instruments Ltd., China) integrated a ns laser beam (λ = 532 nm, 5 ns) with an inverted fluorescence imaging module. The laser beam trajectory encompassed an expanded beam (Lens 1, focal length f = 15 mm; Lens 2, focal length f = 50 mm), a half-wave plate, a polarizing beam splitter, and a series of mirrors, ultimately focusing on the micropore array chip through a microscopic objective (Olympus, 10x) mounted on an X-Y stage. A 50x objective was employed to capture the cell morphology under bright field illumination, while fluorescently labeled cells were monitored through a dedicated fluorescent light source. Images were acquired by a charge-coupled device (CCD) camera (Do3think Co. Ltd., China). The sorted cells were received in a 96-well plate, with positioning controlled by an X-Y electronic control stage. Unless otherwise specified, optical elements were purchased from Thorlabs.

Chip Fabrication and Integration. The micropore array chip consists of an aluminum-coated glass substrate, a Parylene micropore membrane and a silicone membrane. The aluminum-coated glass substrate was produced by magnetron sputtering 25-nm thick aluminum on the surface of the glass substrate (75 mm × 25 mm × 1 mm). Fabricating a Parylene micropore membrane involves a multi-step process (25-μm thick, 25-μm in diameter). Initially, photolithography was utilized to pattern the design, followed by dry etching to produce a hexagonal silicon pillar template. Subsequently, Parylene C polymer was deposited onto the template via chemical vapor deposition. The excess Parylene was then removed using dry etching. Finally, wet etching was employed to achieve the desired micropore array structure. For integration, a silicone membrane was used to secure the Parylene micropore membrane on the aluminum-coated glass substrate.

Surface Treatment. First, we fixed the microporous membrane onto the substrate surface and added a quantified amount of droplets, which did not disperse and maintained a contact angle CA=133.45. Subsequently, we treated the substrate with plasma to alter its hydrophilicity, achieving a superhydrophilic surface. Despite this treatment, the droplet did not disperse when placed on the micropore membrane on the treated glass substrate. Therefore, modifying the microporous membrane became crucial. We masked one side of the microporous membrane to retain its original hydrophobicity while treating the other side with plasma. We then combined the membrane with treated and untreated substrates, naming them Chip 1 and Chip 2, respectively.

Fluid Tracking Imaging. We replaced the metal-coated chip with a glass chip for enhanced microscopic imaging, as the hydrophilic effects induced by plasma treatment on different surfaces are analogous.19 We adjusted the power, airflow, and duration of the plasma treatment to approximate the hydrophilic effects of both substrates. First, a homogeneous mixture of Rhodamine B solution at a concentration of 0.2 g/L was prepared. Subsequently, plasma treatment was applied to the Parylene membrane, which was then affixed onto the treated and untreated glass chip surfaces using a silicone membrane. A volume of 7 μL of the solution was dispensed onto each chip, and imaging was conducted using an S3000 confocal fluorescence microscope with both upright (40x objective) and inverted (20x objective) configurations. Finally, the acquired images were processed using Imaris Viewer.

Cell Culture. Human lung adenocarcinoma cells (PC-9 cell line, FuHeng, China) were cultured in RPMI 1640 medium (Gibco, USA) supplemented with 10% fetal bovine serum (Gibco, USA) and 1% penicillin/streptomycin (Gibco, USA). The working concentrations used in the 1% supplement are 100 units/mL penicillin and 0.1 mg/mL streptomycin. During routine cell culture, the cells were maintained at 37°C in a 5% CO_2 atmosphere and subcultured upon reaching 80% confluency. The cells were detached from the culture flasks for passaging using a 0.25% Trypsin-EDTA solution (Gibco, USA).

Finite Element Simulations. We conducted finite element simulations using the COMSOL Multiphysics platform. This was achieved by combining the "moving mesh," "laminar flow," "phase field," and "multiphysics" interfaces. We established a relationship function between velocity, time, and space. We simplified the liquid domain within the micropores as cuboids with dimensions of 12.5 μm in length and 25 μm in thickness. In comparison, the gas domain was represented by rectangular cuboids with dimensions of 16.5 μm in length and 75 μm in thickness. The model was constructed using a two-dimensional axisymmetric approach for instantaneous solving. The physics of the liquid transfer driven by the instant vaporization of the Al metal film under the action of a pulsed laser in the micropores was replicated, thereby capturing the dynamic changes in micropore sorting.[11, 12] We also employed the heat transfer module of COMSOL Multiphysics to construct a temperature distribution model of the sorting process.[13] The parameters set included a metal absorption coefficient of 0.088, a metal thickness of 25 nm, a pore diameter of 25 μm, a laser

spot size of 5 μm, and a pulsed laser energy of 350 nJ. In this model, the transient heat generated by the 5 ns pulsed laser beam acting on the aluminum-coated metal film caused the surrounding liquid to heat up, leading to temperature diffusion within the micropores. We assessed the thickness parameters based on the temperature diffusion range, time, and temperature change relationship to ensure that the sorting process at this thickness would not adversely affect the viability of cells within the micropores.

Single Cell Isolation. A concentration of 10^6 cells/mL is optimal for mammalian cell suspensions, supporting adequate cell viability and serving as a recommended standard for various downstream applications, including sorting, counting, and resuspension.[14] Therefore, we employed PC-9 cells at an initial concentration of 5×10^5 cells/mL, which were subsequently concentrated 2-fold, 5-fold, and 10-fold to assess isolation efficiency. Subsequently, we aliquoted 7 μL of each concentration onto the micropore sorting chip using a micropipette. Imaging was conducted at five randomly chosen positions (top, bottom, left, right, and center) on the chip, and this process was repeated thrice. The acquired images were analyzed using ImageJ to determine the efficiency of single-cell capture by comparing the number of micropores containing individual cells to the total number of micropores containing cells.

Automated Single Cell Sorting. Before the sorting experiments, the apparatus was cleaned with hypochlorous acid and 75% alcohol and exposed to ultraviolet light for 30 minutes to eliminate bacterial contamination. Subsequently, the micropore membrane was plasma-treated using O_2 under 200 W, 400 sccm, and 1.5 minutes. The treated micropore membrane and metal-coated chip were subjected to UV sterilization for 30 minutes. Subsequently, cellular treatment was conducted, followed by cell counting and assessment of cell viability utilizing trypan blue staining. Following assembly of the chip, the suspension of cells, prepared in advance, was pipetted onto the chip for single-cell capture. The chip was then placed on a 3D motion platform, while a 96-well plate was positioned on the receiving device. The precise localization of target cells was determined based on real-time images collected by a CCD camera and computer. With a single click, individual cells were separated into the 96-well plate.

Plasmid Transformation and Extraction. The overexpression plasmid for CLIC4 was designed using the Pcmv6 vector and tagged with GFP. Plasmids were procured by Miaoling. *Escherichia coli* DH5α was selected as the host strain, with kanamycin (25 μg/mL) as the antibiotic. Initially, 20 μg of plasmid powder was dissolved in 100 μL of sterile water. Then, 1 μL of the plasmid solution was added to 50 μL of competent cells and incubated on ice for 40 minutes, followed by a 2-minute heat shock at 42 °C and a 2-minute ice bath. The mixture was then added to 500 μL of Lysogeny broth (LB) and shaken for 60 minutes. Subsequently, 50 μL of the mixture was spread onto LB agar plates supplemented with kanamycin and incubated at 37 °C for 12 hours. Single clones were picked and expanded in overnight cultures. Plasmid extraction was performed using the SPARKeasy Kit (SparkJade, AD0103). To linearize the plasmid, plasmids were digested with DraIII and P, and then linear DNA was purified with a QIAquick gel extraction kit (Qiagen 28704).

Cell Transfection. Cell transfection was conducted using Lipofectamine™ 3000 Reagent (Invitrogen). Cells were seeded in 6-well plates and transfected with 5 μg linear DNA for each well when the cell growth density reached approximately 70–80%. Transfection was performed per the manufacturer's instructions for Lipofectamine™ 3000 Reagent (Invitrogen). After transfection, cells were placed in a cell culture incubator overnight. The next day, the medium was replaced with a complete medium containing 400 μg/mL of G418, and cells were further cultured for 48 hours before being harvested for cell line selection.

Image Processing and Statistical Analysis. Fluorescence microscopy images were acquired utilizing confocal fluorescence microscopy, S3000 (HOOKE Instruments Ltd., China). The acquired image data were processed through the ImageJ software (National Institutes of Health, USA). The comprehensive data analysis for the present study was performed employing the OriginPro 2024 software (OriginLab Corporation, Northampton, MA, USA).

Single-Cell RNA Sequencing. For scRNA-seq generated in this work, we used a modified Smart-seq2 protocol.[15-17] Smart-seq2 employs laser-assisted single-cell sorter and micromanipulation for cell sorting, with a volume not exceeding 0.5 μL. Sorted cells were directly transferred to cell lysis buffer for cell lysis. Oligo(dT) primers were used to reverse RNA transcription with polyA tails. Due to a specialized reverse transcriptase, three Cs were added to the 3' end of the cDNA chain. The cDNA double strands were synthesized using a TSO primer, displacing RNA complementary to the single-stranded cDNA. Subsequent PCR amplification amplified cDNA to the nanogram level. DNA was fragmented using modified high-activity Tn5 transposase while adapters were added to both cDNA ends—finally, adapter amplification for next-generation sequencing completed library construction. For subsequent analysis, read sequences were aligned with the human RefSeq reference genome (GRCh38).

RESULTS AND DISCUSSION

Design and Working Principle. The micropore array chip consists of three main elements, *i.e.*, a Parylene micropore membrane, an aluminum-coated glass substrate and a silicone membrane (**Figure 1a**). The micropore membrane is patterned to achieve single-cell isolation, and the glass substrate is coated with a layer of aluminum to facilitate the LIFT process. The micropore membrane and the aluminum-coated glass substrate are then assembled via the silicone membrane. The Parylene micropore membrane (10 mm × 10 mm) comprises over 120000 spatially distributed hexagonal micropores.[18] Each micropore has a side length of 12.5 μm, a thickness of 25 μm, and a 4-μm gap between adjacent pores (**Figure 1b**). The diagonal length of the micropores (25 μm) is comparable to the size of single cells (10 – 20 μm), improving the efficiency of single-cell isolation. The micropores are arranged in a hexagonal packing pattern, and the hydrophilicity of the micropore membrane is modified through plasma pretreatment to ensure rapid single-cell isolation.[19, 20] The sample loading process is straightforward, whereby a precise volume of cell suspending medium is first added onto the micropore array chip. Rapid dispersion of the medium forms various picoliter droplets in the micropores, facilitating efficient single-cell isolation

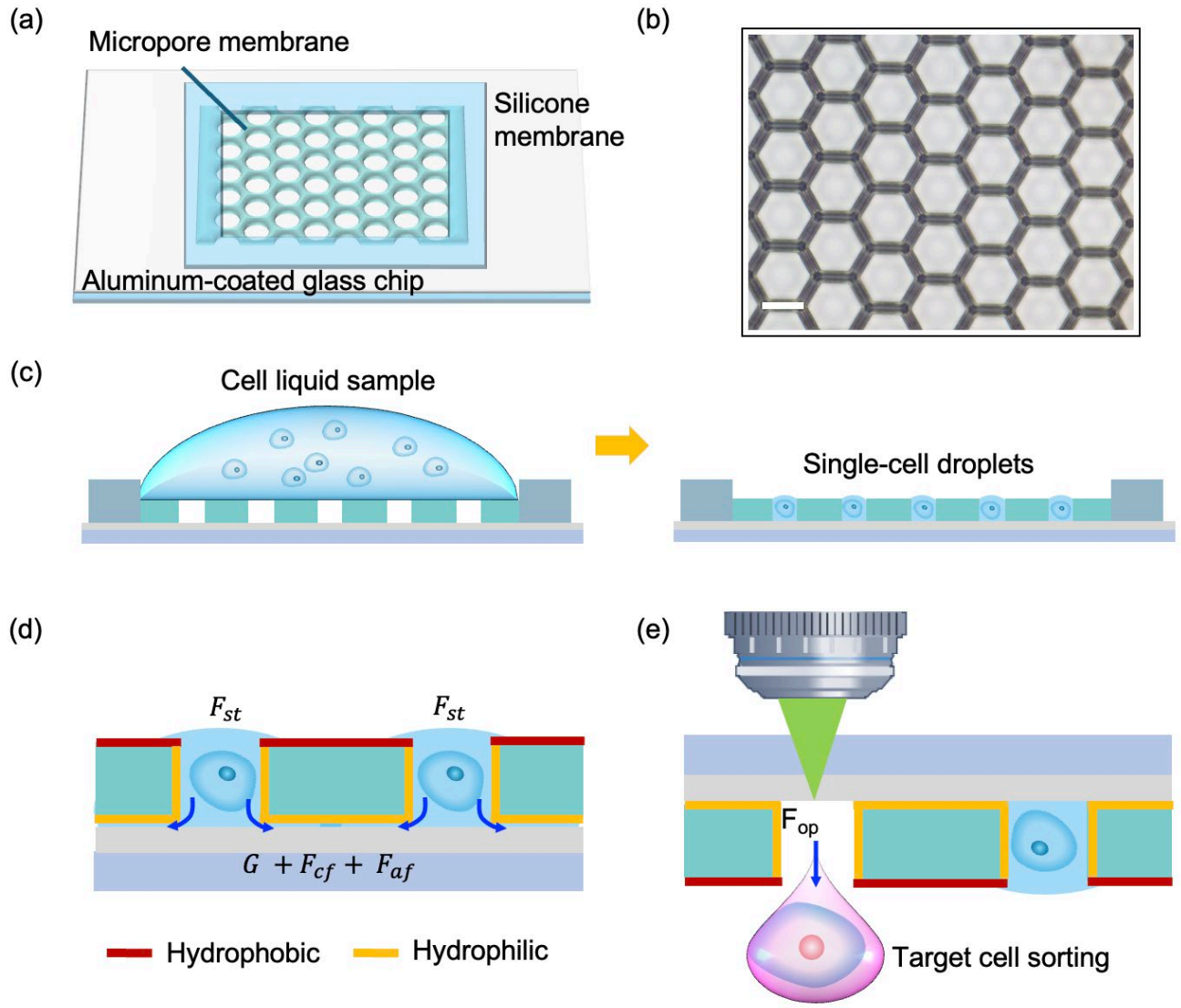

Figure 1. Schematic and working principle of the laser-assisted single-cell sorter. (a) A micropore array chip consisting of a micropore membrane for single-cell isolation. **(b)** Micrograph of fabricated micropore membrane. Scale bar denotes 20 μm. **(c)** Illustration depicting the initial and final state of cell droplet deposition onto the micropore array chip led to single cell isolation on each micropore. **(d)** Force analysis on the cell droplet. **(e)** Illustration of single-target cell release operation for target cell sorting based on laser-induced forward transfer through the interaction of a pulsed laser with the metal film, generating a pushing optical force to release the target cell droplet onto a 96-well plate.

(**Figure 1c**). The single-cell droplet formation within the micropores is based on the combined effects of gravitational force (G), capillary force (F_{cf}), adhesion force (F_{af}), and surface tension force (F_{st}) (**Figure 1d**), as described by the following equations, respectively.

$$G = m \cdot g \tag{1}$$

$$F_{cf} = 2 \cdot \pi \cdot r \cdot \gamma \cdot \cos(\theta) \tag{2}$$

$$F_{af} = \gamma_{sf} \cdot A \cdot \cos(\theta) \tag{3}$$

$$F_{st} = \gamma \cdot L \tag{4}$$

where m is the mass of the liquid, g is the acceleration due to gravity, r is the radius of the capillary, γ is the surface tension coefficient of the liquid, θ is the contact angle, γ_{sf} is the surface energy of the solid-liquid interface, A is the contact area between the solid surface and the liquid, and L is the length of the liquid surface. Adhesion force (F_{af}) is the attraction force acted on the liquid molecules with a hydrophilic surface. On a hydrophilic-treated surface like Parylene, the water molecules will experience an attractive force that causes the liquid to spread over the surface. Capillary force (F_{cf}), on the other hand, occurs when the liquid rises (or is drawn) into a narrow space due to the balance of cohesive forces within the liquid and adhesive forces between the liquid and the solid surfaces. In the micropore setup, this force helps draw liquid into the micropores of the membrane if the adhesion between the liq-

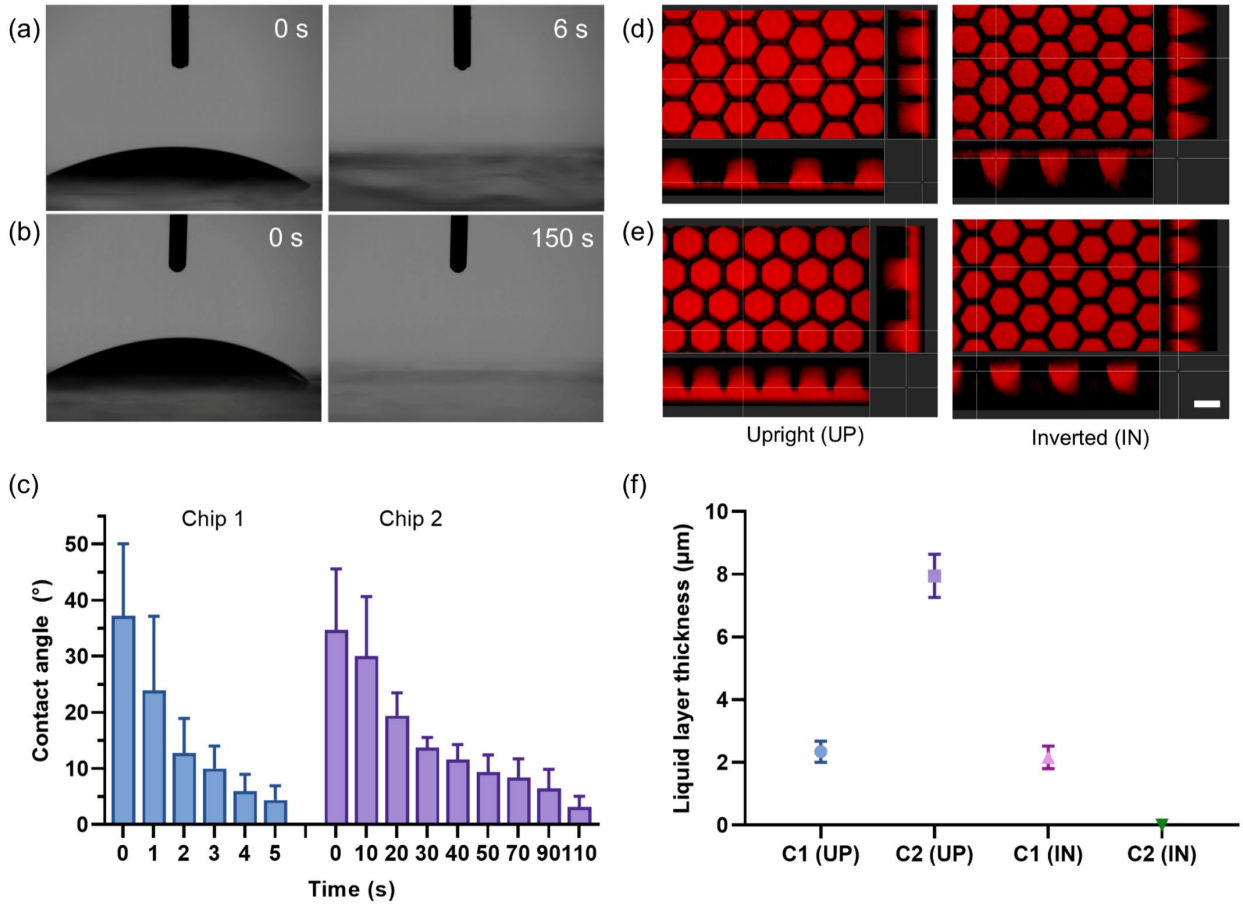

Figure 2. Effect of hydrophilicity of micropore array chip. (a) Images of a liquid droplet initially formed on Chip 1 and after 6 s. **(b)** Images of a liquid droplet initially formed on Chip 2 and after 150 s. **(c)** Contact angle measurements over time of a liquid droplet on Chip 1 and 2. Error bars represent standard deviation of three repetitive measurements. Confocal microscopic images of liquid droplets formed in the micropore array of **(d)** Chip 1 and **(e)** Chip 2 when the chip is placed upright and inverted. Scale bar denotes 20 µm. **(f)** Liquid layer thickness between the micropore array and aluminum-coated glass substrate of Chip 1 (C1) and Chip 2 (C2) under upright (UP) and inverted (IN) positions. Error bars represent standard deviation of ten repetitive measurements.

uid and the solid is stronger than the cohesive forces between liquid molecules. The combined effects of gravity (G), capillary, and adhesion forces disrupt the surface tension (F_{st}) of the liquid layer, as shown by $G + F_{cf} + F_{af} > F_{st}$ (**Figure 1d**), causing the cell sample liquid to spread rapidly and be pulled toward the micropores, generating picoliter droplets in the micropores.[21] Cells are randomly distributed in the micropore array, following a Poisson distribution, whereby most of the micropores consist of a single cell with a chosen optimum cell concentration condition. Subsequently, the micropore array chip is inverted and placed onto an in-house optical microscopic system for target cell sorting (**Figure S1**). The optical microscopic system consists of two subsystems. First, an inverted optical microscopic imaging system is designed to identify individual target cells from heterogeneous cell populations based on cell morphology (bright-field) or molecular profiling (fluorescence). Targeted cells can be retrieved through the LIFT microscopic system for downstream cell culture or analysis, such as RNA sequencing. In the LIFT microscopic system, a 532-nm pulse laser is focused onto one of the micropores with the target cell droplet through an objective lens, whereby the interaction between photons and the material induces optical breakdown. This creates rapidly expanding cavitation bubbles at the focal point, generating a liquid jet that transfers the single target cell to one of the wells on a 96-well plate (**Figure 1e**). As a result, both highly efficient and automated single-cell isolation and precise single-target cell sorting are achieved, facilitating subsequent selective single-cell analysis.

Effect of Hydrophilicity. To investigate the effect of the surface hydrophilicity of the micropore array chip on the single-cell isolation process, we treated the aluminum-coated glass substrate or the micropore membrane with plasma[22] to alter its hydrophilicity, achieving super hydrophilic surfaces **(Figure S2)**. Two types of micropore array chips were tested, *i.e.*, plasma-treated micropore membrane assembled with treated glass substrate (Chip 1) or untreated glass substrate (Chip 2). The contact angle was monitored and measured when a liquid droplet was dropped onto both chips. **Figure 2a** shows that the contact angle of the liquid droplet on Chip 1 was initially 37.2° ± 12.8° and then rapidly spread on the surface within 6 s (a contact angle of 4.4° ± 2.5° at t = 5 s). On the other hand, the initial contact angle of the liquid droplet on Chip 2 was 34.7° ± 10.9°, as illustrated in **Figure 2b**, and spread slower than Chip 1 (**Figure 2c**). Ultimately, the liquid droplet also spread onto the surface of Chip 2 after 2.5 min, achieving a contact angle of 3.1° ± 1.9° at t = 110 s. This indicates that plasma-

treated hydrophilic surfaces (side walls and bottom surface) of the micropore membrane enhance the attraction of water molecules, disrupting the liquid surface tension force (F_{st}) under the combined effects of gravitational force (G), adhesion force (F_{af}), and capillary force (F_{cf}) (**Figure 1d**).[23-25] The untreated hydrophobic top surface of the micropore retains its original properties, repelling the water molecule and preventing liquid layer formation. Therefore, during sample loading, the micropore membrane plays a crucial role in disrupting the liquid layer on its top surface, facilitating single-cell isolation.

We further analyzed the liquid droplets formed in the micropore array of both chips and the effect of different chip positions (upright and inverted). Rhodamine B was used as a liquid tracer, and a confocal fluorescence microscope was used to image the 3D distribution of the liquid in the micropore membrane.[26] **Figure 2d** shows that Chip 1 retained a liquid layer between the micropores and the treated glass substrate in both upright and inverted positions. In contrast, **Figure 2e** indicates that Chip 2 only exhibited a liquid layer in the upright position but not in the inverted position. The liquid layer thickness in Chip 1 was significantly smaller than that of Chip 2 in the upright position, with an average thickness of 2.3 μm ± 0.3 μm for Chip 1 and 7.9 μm ± 0.7 μm for Chip 2, as shown in **Figure 2f**. These findings suggest that the hydrophilically treated aluminum-coated glass surface exhibits greater attraction force towards water molecules, promoting liquid spreading, reducing the contact angle, and decreasing the thickness of the liquid layer between the micropores and the glass substrate.[23]

On the other hand, Chip 1 maintained a liquid layer with an average thickness of about 2.2 μm ± 0.4 μm in the inverted position. In contrast, no significant liquid layer was observed on Chip 2. These data indicate that when the chip is inverted, the direction of gravitational force changes, exerting a downward force on the liquid layer. Combined with the changed direction of capillary force, this force opposes and disrupts the liquid surface tension and adhesion force. The hydrophilically treated surface in Chip 1 has a smaller contact angle, increasing the capillary and adhesive forces. This results in better liquid spreadability on the surface, increased surface energy γ_{sf}, and a more stable liquid layer that is less likely to separate under the influence of gravity. Conversely, the untreated surface has a larger contact angle, reducing both capillary and adhesive forces. Consequently, the liquid has poorer spreadability, decreased surface energy γ_{sf} and a less stable liquid layer that is more prone to separation due to gravity G. The relevant equation can be expressed as

$$\Delta h \propto \frac{F_{af}+F_{cf}}{G} \quad (5)$$

where Δh represents the change in the liquid layer thickness. On the hydrophilically treated surface, due to the larger F_{af} and F_{cf}, Δh is smaller, indicating a smaller change in the liquid layer thickness. In contrast, on the untreated surface, the smaller F_{af} and F_{cf} result in a larger Δh, indicating a greater change in the liquid layer thickness, manifesting as the rapid thinning of the liquid layer. In summary, the thinner liquid layer requires overcoming less surface tension, which is beneficial for reducing the energy threshold needed for subsequent single-cell droplet sorting and releasing. Chip 2 that combines a single-sided hydrophilic-treated Parylene micropore membrane with an untreated aluminum-coated glass substrate offers a better option for single-cell isolation and sorting with overall enhanced efficiency.

Single-Cell Isolation and Sorting. To characterize the performance of single-cell capture, we conducted imaging and counting of PC-9 cells captured at different concentrations on the micropore array chip (**Figure 3a**). To validate the isolation of individual cells within the micropores, we employed confocal fluorescence microscopy scanning imaging to visualize the positions of cells in the micropores. The PC-9 cells were labeled with a membrane stain that exhibits green fluorescence. Through cross-sectional profiling (**Figure 3b**), we confirmed that the PC-9 cells were isolated inside the micropores. We then determined the single-cell isolation efficiency by calculating the ratio of micropores containing a single cell to the total number of cells captured by the micropores. **Figure 3c** illustrates that, with a concentration of 5×10^5 cells/mL, the single-cell isolation efficiency was 81.83% ± 3.97%. By increasing the cell concentration up to 5×10^6 cells/mL, the single-cell isolation efficiency still consistently remained above 80%. Calculations indicate that at a concentration of 10^7 cells/mL, the number of cells approaches the number of micropores, leading to a significant drop in efficiency at this and higher concentrations. When the target sample is abundant, we recommend diluting the sample to the optimal concentration of 5×10^6 cells/mL to maintain high single-cell isolation efficiency. These findings validate the mechanism of single-cell isolation and are conducive to the accuracy of subsequent single-cell sorting and the efficiency of downstream single-cell analysis.

To comprehend the microscale processes involved in single target cell sorting, we simulated the dynamic changes in liquid sorting in Chip 1 and Chip 2, and the liquid jetting processes were illustrated in **Figure S3**. We observe that the liquid jetting process in Chip 2 is notably faster, with less droplet deformation and smaller tension hindrance than in Chip 1. This indicates that hydrophilic-treated glass substrate exhibits greater attraction force to water molecules than untreated chips, impeding liquid jetting. These findings further confirm that Chip 2 is more conducive to subsequent single-cell sorting, aiding in maintaining cell viability. Like all laser-induced processes, the increased temperature on the acting site and its diffusion distribution are critical to cell viability. To optimize the suitable thickness of the micropores, we simulated the temperature diffusion distribution within the micropores when the micropore array chip was subjected to the pulsed laser. The temperature simulation results illustrate the heat transfer from the aluminum coating to the liquid domain under brief pulsed laser exposure, analyzing the effect of temperature changes at different locations within the liquid domain on the cells, in which the high reflectivity of aluminum ensures that short-pulse laser exposure causes negligible photoradiation damage to the cells. **Figure S4** illustrates the temperature diffusion within the liquid domain along the micropore at different time points, with a maximum temperature reaching approximately 6.28×10^3°C at the focal point of the pulsed laser, *i.e.*, the interface between the aluminum layer and the micropore. The increased temperature is confined within the range of 3 μm during the extremely brief pulsed laser exposure, with temperatures in the surrounding liquid domain re-

maining below 37°C. As most human cells require an incubation temperature of ~ 37°C,[27] cells remain unaffected when they are away from the focal point of the pulsed laser. When the micropore array chip is in an inverted position, cells are typically positioned away from the laser focal point due to gravitational effects. To ascertain the actual position of an isolated cell in a micropore, we obtained the cross-sectional image of the cell using a confocal fluorescence microscope. **Figure S5** shows that the single cell was located 10 μm from the metal surface, further than the temperature-affected range (within 3 μm). Since most cells fall in the range of 10 to 20 μm, the thickness of the micropore will be chosen to be slightly larger than that (25 μm in our case). This effectively prevents thermal damage of the cells from the LIFT process, supporting cell viability and facilitating downstream single-cell analysis.

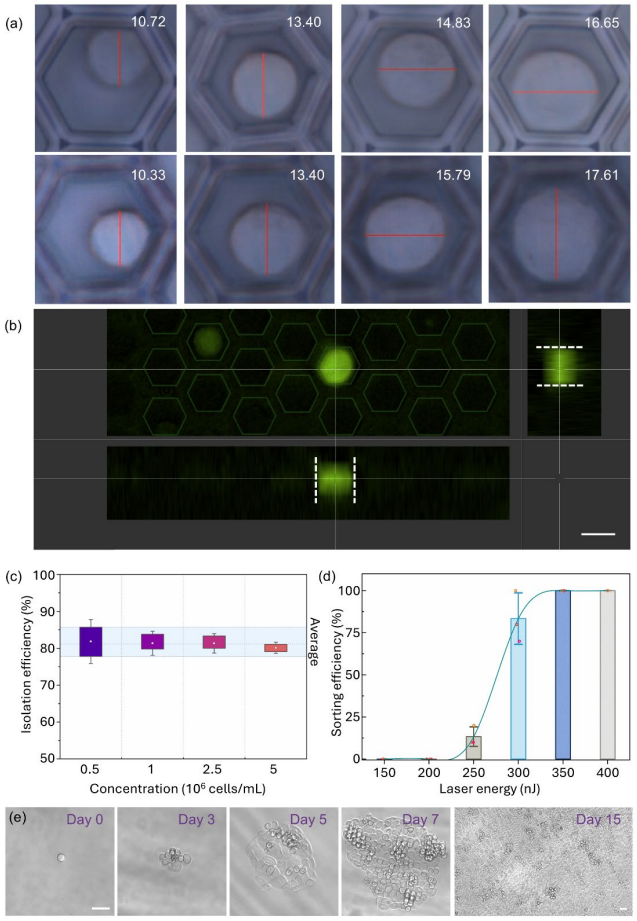

Figure 3. Single-cell isolation. (a) Images of single PC-9 cell isolation on different micropores. Diameter of each cell is shown. **(b)** Confocal image of a single PC-9 cell being isolated in a micropore. Scale bars denote 20 μm. **(c)** Single-cell isolation efficiency with different cell concentrations. **(d)** Sorting efficiency of single target cell under different laser energies. **(e)** Microscopic images depicting the culture of a single PC-9 cell at various time points after being sorted by the laser-assisted single-cell sorter. Scale bars denote 50 μm.

Next, we investigated the sorting efficiency of single PC-9 cells under different laser energies from 150 nJ to 400 nJ and used glass slides to retrieve the ejected cell droplets from the micropores. 10 PC-9 cells were sorted in each experiment, and the experiments were repeated thrice for each laser energy. The sorting efficiency was calculated as the number of successful receptions divided by the total number of sorted cells. The results (**Figure 3d**) show that the sorting efficiency increased with laser energy, reaching approximately 100% at a minimum threshold energy of 350 nJ. Temperature simulation results confirmed that this energy level represents a favorable threshold for efficient and cell-friendly sorting. The sorting process utilizes pulsed laser applied to a metal film to transfer single-cell droplets from micropores to a 96-well plate. Notably, the sorting energy threshold used in our experiments is significantly lower than that typically required for laser printing,[28] minimizing the impact of laser energy settings on sorting different cell types. To validate the impact of sorting on cell viability, we cultured each cell separately after sorting 24 single cells individually into a 96-well plate containing culture medium at a laser energy of 350 nJ. The entire experiment was

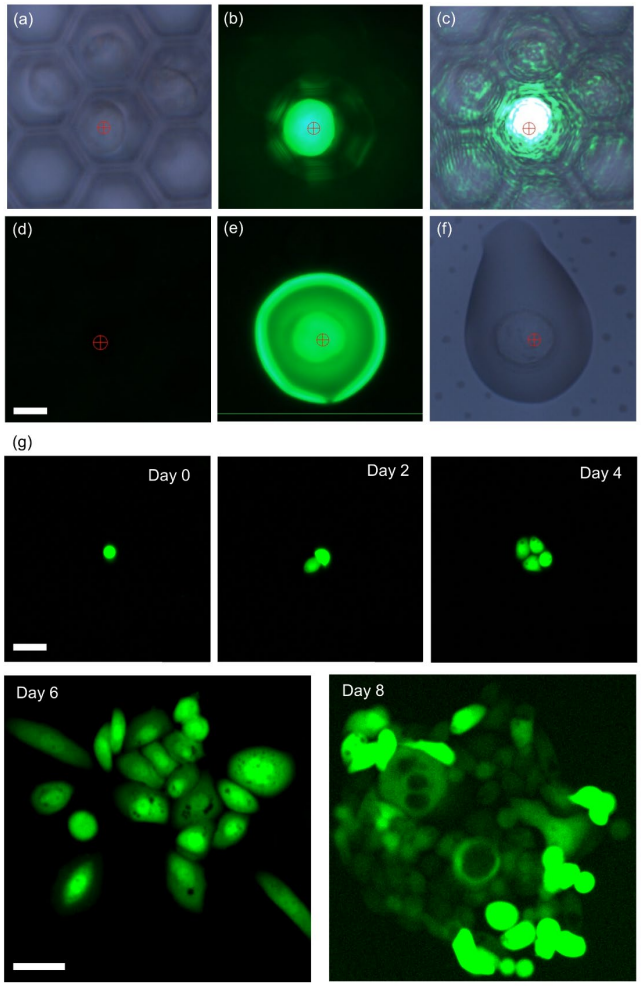

Figure 4. Transfected cell sorting. (a) Brightfield image, **(b)** fluorescent image, and **(c)** laser overlay image of a target cell for sorting. Fluorescence image of the receiver well **(d)** before and **(e)** after target cell sorting. **(f)** brightfield image of the coverslip after target cell sorting. Scale bar denotes 10 μm. **(g)** Fluorescence microscopic images illustrating the growth status of an individual target cell at various time points post-sorting via the laser-assisted single-cell sorter. Scale bar denotes 50 μm.

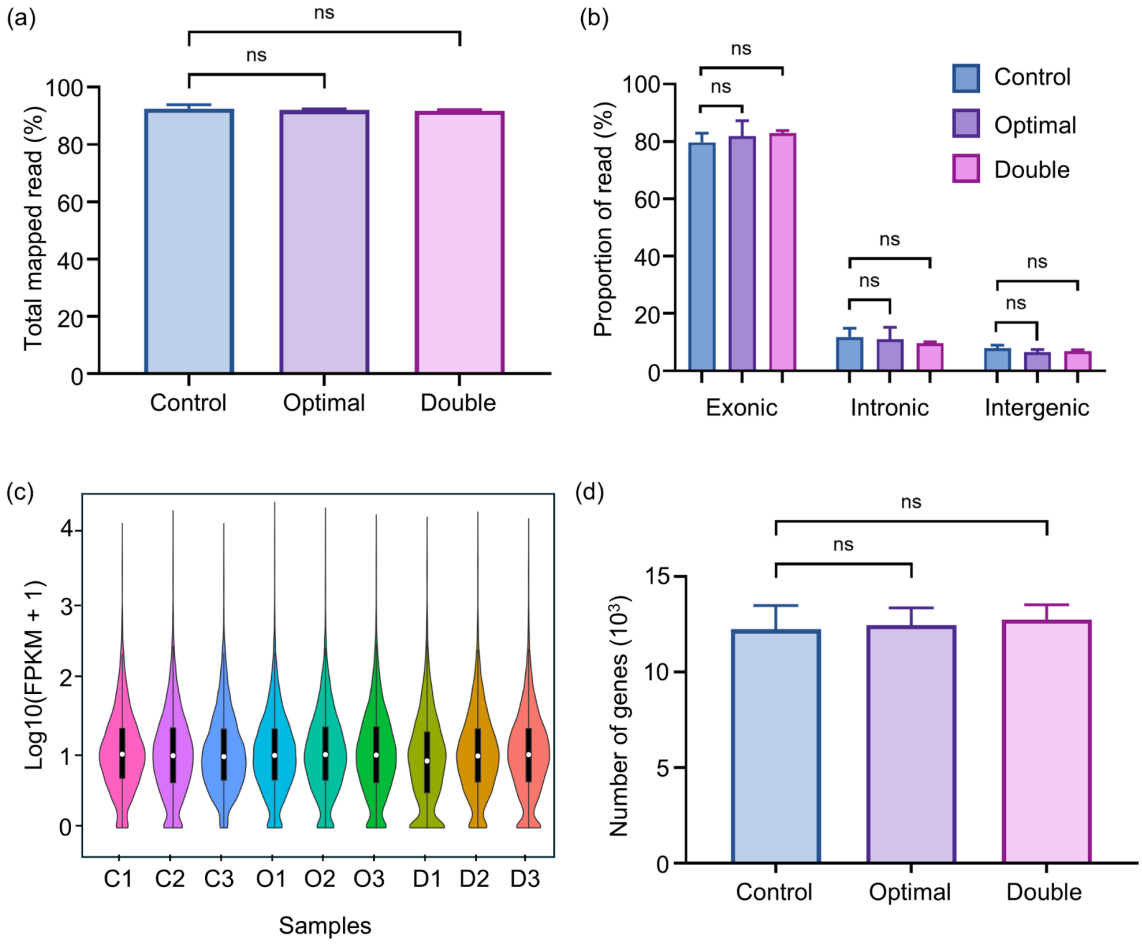

Figure 5. Single-cell RNA sequencing comparison. (a) Percentage of total mapped reads obtained from RNA sequencing with reads from the reference genome using micromanipulation technique (Control), laser-assisted single-cell sorter at optimal energy 350 nJ (Optimal), and at higher energy 800 nJ (Double). **(b)** Proportion of reads mapped to exonic, intronic, and intergenic regions calculated based on alignment results. **(c)** Distribution graph of all gene expression. **(d)** Distribution graph of the number of genes. For **(a, b and d)**, n. s.: not significant, * p<=0.05, ** p<=0.01, *** p<=0.001. Error bars represent standard deviation of three repetitive experiments.

repeated thrice. The viability of single-cell sorting was determined by calculating the ratio of successfully cultured cells to the total number of sorted cells, which was 79.2% ± 4.2%. Concurrently, we monitored the growth of individual cells over time using the optical microscopic system (**Figure 3e**). These results further validate the simulation results and showcase the high isolation and sorting efficiencies of the laser-assisted single-cell sorter with high cell viability capability, rendering it an indispensable new technique in cellular engineering.

Transfected Cell Sorting and Culture. To validate the functionality of the laser-assisted single-cell sorter, we utilized it to rapidly and precisely isolate rare single cells from a population of transfected cells. First, PC-9 cells were transfected with PCMV6-CLIC4-GFP to generate a heterogeneous cell population, with or without overexpressing CLIC4-GFP. Fluorescence microscopy was employed to monitor the post-transfection cell growth. Images were captured from different positions (top, bottom, middle, left, and right) to assess the proportion of successfully transfected target cells, which ranged from 1% to 5% of the total cell population (about 5×10^5 cells). Next, transfected heterogenous PC-9 cells were loaded onto micropore array chips, and single-cell isolation was conducted, followed by real-time visualization and rapid targeting of target cells. Target cells were then sorted into individual wells of a 96-well plate using a laser energy of 350 nJ. All wells were filled with the culture medium G418, and cell growth was monitored. To demonstrate the sorting process, we used a coverslip as the receiver. **Figures 4a-c** show a target cell in a micropore. **Figure 4d** shows an empty coverslip before the single target cell sorting. With the pulse laser, the cell droplet was ejected from the micropore and received on the coverslip. Comparing the pre-sort empty receiver with the post-sort receiver, we confirmed the acquisition of the single target cell (**Figures 4e-f and Movie S1**). Subsequently, we cultured the single target cell and monitored its growth status. **Figure 4g** displays the growth status of the target cell at different time points, confirming the reliability of the laser-assisted single-cell sorter in maintaining cell viability. The entire process of isolating target cells meets the requirements for real-time imaging, precise localization, and one-step separation of actual rare target cell samples. This approach minimizes cell loss and the risk of contamination during sorting and facilitates downstream single-cell research.

Table 1. Comparative analyses of our method with other techniques.

Sorting Method	Single-Cell Sorting Accuracy	Throughput	Cell Damage	Cost-Efficiency in Sequencing	References
Fluorescence-activated cell sorting	Low	High, 10^2-10^5 events/s	High Potential for cell damage due to shear stress and laser exposure	High Additional costs due to low sorting accuracy	9, 32, 33
Micromanipulation	High, >90%	Low, limited to manual or semi-automated systems	Low Manual or robotic contact with minimal force	Low	34
Droplet Microfluidics	Moderate, 90%	High, 130 μL/min	Low Confined in microdroplets with minimal shear	Moderate	35
Dielectrophoresis	Moderate, 91.5%	Moderate, 6 000 cells/h	Low to moderate Depending on the strength of the electric field used	Moderate	36, 37
Acoustic Sorting	Moderate, 85%	High, 500 μL/min	Low Manipulated using acoustic waves with no direct contact	Moderate	38
Automated laser-assisted single-cell sorting	High, ~100%	Moderate, >10^3 cells/h	Low Microbubbles with no direct contact	Low	This work

Single-Cell RNA Sequencing. To evaluate the impact of the laser-assisted single-cell sorter on cell transcriptional profiles during cell sorting, we performed single-cell SMART-seq on individual cells sorted by (1) gentle micromanipulation technique (Control), the laser-assisted single-cell sorter with (2) optimal sorting energy of 350 nJ (Optimal) and (3) higher energy of 800 nJ (Double). Since micromanipulation is currently the gentlest single-cell sorting method without causing significant cell damage, we used micromanipulation as a control method to evaluate the impact of the laser-assisted single-cell sorter on single-cell RNA sequencing. **Figure 5a** shows the percentages of total mapped read, which are all above 91% in all three cases, showing no significant difference between these cases. Furthermore, the distributions of reads (**Figure 5b**) mapped to different regions (exonic, intronic and intergenic) and gene expression (**Figure 5c**) are also consistent in all cases. Most importantly, the total detected number of genes is comparable between the cells sorted by the three techniques (**Figure 5d**). Given that RNA sequencing requires high cell viability,[29] these results indicate that the laser-assisted single-cell sorter provides efficient and stable single-cell transcriptome information during cell sorting and maintains a safe energy threshold of up to 800 nJ. This broadens its applicability to isolate and sort larger cells that require higher laser energy. Future works could be focused on determining the laser energy threshold for other cell types such as primary cells or bacterial cells. As a result, the laser-assisted single-cell sorter has demonstrated highly efficient single-cell isolation and sorting with highly accurate downstream single-cell analysis as compared to gentle micromanipulation technique, avoiding additional costs associated with low sorting accuracy and cell viability as in FACS. Our method also offers higher flexibility in single cell sorting as compared to acoustic technology. Although acoustic technology is a fast, reproducible, and gentle method for cell sorting, the sorting efficiency might be low, particularly when separating cells with similar acoustic properties (e.g., size and density), and it could be affected by interference from other cells or microbubbles.[30, 31] Table 1 illustrates comparative analyses of our method with other techniques. Our technology offers high precision in single-cell sorting with minimal damage, making it suitable for efficient single-cell RNA sequencing analysis while reducing the costs, which is highly beneficial for researchers. Although sorting throughput is limited by the mechanical platform, integrating algorithms for fully automated operation will make this technology a valuable tool for biological research and precision medicine.

CONCLUSIONS

We demonstrate an automated laser-assisted single-cell sorter, which enables efficient high-throughput single-cell isolation in a surface-functionalized micropore array chip and precise single-cell sorting based on LIFT technology, facilitating practical downstream single-cell analysis by maintaining cell viability. The laser-assisted single-cell sorter with over 80% single-cell isolation efficiency offers clear advantages over traditional manual micromanipulation, which is laborious and suffers from low efficiency and low throughput. In addition to high throughput, the micropore array chip contains hundreds of

thousands of spatially segregated micropores, combined with the high spatial resolution provided by fluorescence microscopy to enhance the multiplexing capabilities of micropore assays. The laser-assisted single-cell sorter offers several additional distinctions compared to FACS, including the ability of direct cell imaging, leading to accurate and robust isolation of single cells with high precision while maintaining high cell viability (about 80%). Moreover, the laser-assisted single-cell sorter is compatible with a wide range of cell types, including adherent and non-adherent cells, demonstrating superior capabilities as compared to droplet-based microfluidic technology, which suffers from the problem of releasing cells from the emulsion state, causing higher cell loss.[9] Unlike microfluidic-based techniques, which primarily rely on other methods to recover samples, we present a direct laser-based approach for sample recovery that avoids susceptibility to clogging. The laser-assisted single-cell sorter leverages a one-click operation for single target cell sorting, significantly simplifying the technical complexity and enhancing user experience.

We further demonstrate the capability of the laser-assisted single-cell sorter for efficient single-cell culture or RNA sequencing, which is achievable within only 1 or 2 rounds of single-cell sorting, avoiding additional costs due to low sorting accuracy and reduced cell viability. This is evidenced by our rapid isolation of rarely individual transfected cells from heterogeneous cell populations. In summary, the laser-assisted single-cell sorter provides a new approach for efficient identification and precise sorting of single target cells for reliable and accurate single-cell analysis. The laser-assisted single-cell sorter could be broadly applied for various downstream single-cell analyses such as genome sequencing, epigenetic analysis, RNA sequencing, intracellular molecular profiling, cell surface proteome profiling, single-cell functional studies, *etc.*, offering unprecedented insights into cellular diversity and function.

ASSOCIATED CONTENT

Supporting Information.

Additional details. Figure S1 shows the optical microscopic system for single target cell sorting; Figure S2 shows the contact angle measurements; Figure S3 shows the simulation of the liquid jetting process based on the LIFT mechanism; Figure S4 shows the 3D surface mapping of temperature variation in a micropore; Figure S5 shows the confocal cross-sectional image of a cell in a micropore (PDF).

Movie S1 shows the sorting process of individual target cells using the laser-assisted single-cell sorter in transduced cell lines (MP4).

AUTHOR INFORMATION

Corresponding Author

Wei Luo, Email: wei-hc.luo@polyu.edu.hk
Lip Ket Chin, Email: lkchin@cityu.edu.hk
Shilun Feng, Email: shilun.feng@mail.sim.ac.cn
Bei Li, Email: beili@ciomp.ac.cn

Author Contributions

The manuscript was written through contributions of all authors. All authors have given approval to the final version of the manuscript.

Funding Sources

The work was supported by the National Natural Science Foundation of China (Grant No. 62104227).

Notes

The authors declare no competing financial interest.

ACKNOWLEDGMENT

The authors also thank the Peking University National Key Laboratory of Science and Technology technicians on micro/nano fabrication for helping with the processes.

ABBREVIATIONS

LIFT, laser-induced forward transfer; FACS, fluorescence-activated cell sorting; CCD, charge-coupled device; LB, Lysogeny broth.

REFERENCES

(1) Wu, F.; Fan, J.; He, Y.; Xiong, A.; Yu, J.; Li, Y.; Zhang, Y.; Zhao, W.; Zhou, F.; Li, W. Single-Cell Profiling of Tumor Heterogeneity and the Microenvironment in Advanced Non-Small Cell Lung Cancer. *Nat. Commun.* **2021**, *12* (1), 2540.

(2) Kim, N.; Kim, H. K.; Lee, K.; Hong, Y.; Cho, J. H.; Choi, J. W.; Lee, J.-I.; Suh, Y.-L.; Ku, B. M.; Eum, H. H. Single-Cell RNA Sequencing Demonstrates the Molecular and Cellular Reprogramming of Metastatic Lung Adenocarcinoma. *Nat. Commun.* **2020**, *11* (1), 2285.

(3) Zeng, Q.; Mousa, M.; Nadukkandy, A. S.; Franssens, L.; Alnaqbi, H.; Alshamsi, F. Y.; Safar, H. A.; Carmeliet, P. Understanding Tumour Endothelial Cell Heterogeneity and Function from Single-Cell Omics. *Nat. Rev. Cancer* **2023**, *23* (8), 544-564.

(4) Hempel, C. M.; Sugino, K.; Nelson, S. B. A Manual Method for the Purification of Fluorescently Labeled Neurons from the Mammalian Brain. *Nat. Protoc.* **2007**, *2* (11), 2924-2929.

(5) Adan, A.; Alizada, G.; Kiraz, Y.; Baran, Y.; Nalbant, A. Flow Cytometry: Basic Principles and Applications. *Crit. Rev. Biotechnol.* **2017**, *37* (2), 163-176.

(6) Ma, C.; Fan, R.; Ahmad, H.; Shi, Q.; Comin-Anduix, B.; Chodon, T.; Koya, R. C.; Liu, C.-C.; Kwong, G. A.; Radu, C. G. A Clinical Microchip for Evaluation of Single Immune Cells Reveals High Functional Heterogeneity in Phenotypically Similar T Cells. *Nat. Med.* **2011**, *17* (6), 738-743.

(7) Lu, Y.; Xue, Q.; Eisele, M. R.; Sulistijo, E. S.; Brower, K.; Han, L.; Amir, E.-a. D.; Pe'er, D.; Miller-Jensen, K.; Fan, R. Highly Multiplexed Profiling of Single-Cell Effector Functions Reveals Deep Functional Heterogeneity in Response to Pathogenic Ligands. *Proc. Natl. Acad. Sci. U.S.A.* **2015**, *112* (7), E607-E615.

(8) Baret, J.-C.; Miller, O. J.; Taly, V.; Ryckelynck, M.; El-Harrak, A.; Frenz, L.; Rick, C.; Samuels, M. L.; Hutchison, J. B.; Agresti, J. J. Fluorescence-Activated Droplet Sorting (FADS): Efficient Microfluidic Cell Sorting Based on Enzymatic Activity. *Lab Chip* **2009**, *9* (13), 1850-1858.

(9) Miwa, H.; Dimatteo, R.; de Rutte, J.; Ghosh, R.; Di Carlo, D. Single-Cell Sorting Based on Secreted Products for Functionally Defined Cell Therapies. *Microsyst. Nanoeng.* **2022**, *8* (1), 84.

(10) Ding, X.; Peng, Z.; Lin, S.-C. S.; Geri, M.; Li, S.; Li, P.; Chen, Y.; Dao, M.; Suresh, S.; Huang, T. J. Cell Separation Using Tilted-Angle Standing Surface Acoustic Waves. *Proc. Natl. Acad. Sci. U.S.A.* **2014**, *111* (36), 12992-12997.

(11) Moreno-Labella, J. J.; Munoz-Martin, D.; Vallejo, G.; Molpeceres, C.; Morales, M. Influence of the Gap between Substrates in the Laser-Induced Transference of High-Viscosity Pastes. *Materials* **2021**, *14* (19), 5567.

(12) Moreno-Labella, J.; Munoz-Martin, D.; Márquez, A.;

Morales, M.; Molpeceres, C. Numerical Study of Water-Glycerol BA-LIFT: Analysis and Simulation of Secondary Effects. *Opt. Laser Technol.* **2021**, *135*. DOI: 10.1016/j.optlastec.2020.106695.
(13) Liang, P.; Liu, B.; Wang, Y.; Liu, K.; Zhao, Y.; Huang, W. E.; Li, B. Isolation and Culture of Single Microbial Cells by Laser Ejection Sorting Technology. *Appl. Environ. Microbiol.* **2022**, *88* (3), e01165-01121.
(14) Freshney, R. I. *Culture of Animal Cells: A Manual of Basic Technique and Specialized Applications*; John Wiley & Sons, 2015.
(15) Picelli, S.; Faridani, O. R.; Björklund, Å. K.; Winberg, G.; Sagasser, S.; Sandberg, R. Full-Length RNA-Seq from Single Cells Using Smart-Seq2. *Nat. Protoc.* **2014**, *9* (1), 171-181.
(16) Sorek, M.; Oweis, W.; Nissim-Rafinia, M.; Maman, M.; Simon, S.; Hession, C. C.; Adiconis, X.; Simmons, S. K.; Sanjana, N. E.; Shi, X. Pluripotent Stem Cell-Derived Models of Neurological Diseases Reveal Early Transcriptional Heterogeneity. *Genome Biol.* **2021**, *22*, 1-25.
(17) Wang, H.; Gong, P.; Chen, T.; Gao, S.; Wu, Z.; Wang, X.; Li, J.; Marjani, S. L.; Costa, J.; Weissman, S. M. Colorectal Cancer Stem Cell States Uncovered by Simultaneous Single-Cell Analysis of Transcriptome and Telomeres. *Adv. Sci.* **2021**, *8* (8), 2004320.
(18) Chang, T. Y.; Yadav, V. G.; De Leo, S.; Mohedas, A.; Rajalingam, B.; Chen, C.-L.; Selvarasah, S.; Dokmeci, M. R.; Khademhosseini, A. Cell and Protein Compatibility of Parylene-C Surfaces. *Langmuir* **2007**, *23* (23), 11718-11725.
(19) Ma, C.; Nikiforov, A.; Hegemann, D.; De Geyter, N.; Morent, R.; Ostrikov, K. Plasma-Controlled Surface Wettability: Recent Advances and Future Applications. *Int. Mater. Rev.* **2023**, *68* (1), 82-119.
(20) Chytrosz-Wrobel, P.; Golda-Cepa, M.; Stodolak-Zych, E.; Rysz, J.; Kotarba, A. Effect of Oxygen Plasma-Treatment on Surface Functional Groups, Wettability, and Nanotopography Features of Medically Relevant Polymers with Various Crystallinities. *Appl. Surf. Sci. Adv.* **2023**, *18*, 100497.
(21) Urone, P. P.; Hinrichs, R. J. C. P. 11.8 Cohesion and Adhesion in Liquids: Surface Tension and Capillary Action. *College Physics* **2016**.
(22) Lai, J.; Sunderland, B.; Xue, J.; Yan, S.; Zhao, W.; Folkard, M.; Michael, B. D.; Wang, Y. Study on Hydrophilicity of Polymer Surfaces Improved by Plasma Treatment. *Appl. Surf. Sci.* **2006**, *252* (10), 3375-3379.
(23) Liston, E.; Martinu, L.; Wertheimer, M. R. Plasma Surface Modification of Polymers for Improved Adhesion: A Critical Review. *J. Adhes. Sci. Technol.* **1993**, *7* (10), 1091-1127.
(24) Chen, L.; Yang, C.; Xiao, Y.; Yan, X.; Hu, L.; Eggersdorfer, M.; Chen, D.; Weitz, D.; Ye, F. Millifluidics, Microfluidics, and Nanofluidics: Manipulating Fluids at Varying Length Scales. *Mater. Today Nano* **2021**, *16*, 100136.
(25) Zisman, W. Surface Energetics of Wetting Spreading and Adhesion. *Journal of Paint Technology* **1972**, *44* (564).
(26) Paul, R.; Zhao, Y.; Coster, D.; Qin, X.; Islam, K.; Wu, Y.; Liu, Y. Rapid Prototyping of High-Resolution Large Format Microfluidic Device through Maskless Image Guided in-situ Photopolymerization. *Nat. Commun.* **2023**, *14* (1), 4520.
(27) Song, P.; Gao, H.; Gao, Z.; Liu, J.; Zhang, R.; Kang, B.; Xu, J.-J.; Chen, H.-Y. J. C. Heat Transfer and Thermoregulation within Single Cells Revealed by Transient Plasmonic Imaging. *Chem* **2021**, *7* (6), 1569-1587.
(28) Guillotin, B.; Souquet, A.; Catros, S.; Duocastella, M.; Pippenger, B.; Bellance, S.; Bareille, R.; Rémy, M.; Bordenave, L.; Amédée, J. J. B. Laser Assisted Bioprinting of Engineered Tissue with High Cell Density and Microscale Organization. *Biomaterials* **2010**, *31* (28), 7250-7256.
(29) Haque, A.; Engel, J.; Teichmann, S. A.; Lönnberg, T. J. G. m. A Practical Guide to Single-Cell RNA-Sequencing for Biomedical Research and Clinical Applications. *Genome Med.* **2017**, *9*, 1-12.
(30) Ding, X.; Peng, Z.; Lin, S.-C. S.; Geri, M.; Li, S.; Li, P.; Chen, Y.; Dao, M.; Suresh, S.; Huang, T. J. J. P. o. t. N. A. o. S. Cell Separation Using Tilted-Angle Standing Surface Acoustic Waves. *Proc. Natl. Acad. Sci. U.S.A.* **2014**, *111* (36), 12992-12997.
(31) Yang, S.; Rufo, J.; Zhong, R.; Rich, J.; Wang, Z.; Lee, L. P.; Huang, T. J. J. N. P. Acoustic Tweezers for High-Throughput Single-Cell Analysis. *Nat. Protoc.* **2023**, *18* (8), 2441-2458.
(32) Hewitt, Z.; Forsyth, N.; Waterfall, M.; Wojtacha, D.; Thomson, A.; McWhir, J. J. C.; Cells, S. Fluorescence-Activated Single Cell Sorting of Human Embryonic Stem Cells. *Cloning Stem Cells* **2006**, *8* (3), 225-234.
(33) Sutermaster, B. A.; Darling, E. M. J. S. r. Considerations for High-Yield, High-Throughput Cell Enrichment: Fluorescence Versus Magnetic Sorting. *Sci. Rep.* **2019**, *9* (1), 227.
(34) Francz, B.; Ungai-Salánki, R.; Sautner, É.; Horvath, R.; Szabó, B. J. M.; Nanofluidics. Subnanoliter Precision Piezo Pipette for Single-Cell Isolation and Droplet Printing. *Microfluidics and Nanofluidics* **2020**, *24*, 1-10.
(35) Chen, Y.-H.; Pulikkathodi, A. K.; Ma, Y.-D.; Wang, Y.-L.; Lee, G.-B. J. L. o. a. C. A Microfluidic Platform Integrated with Field-Effect Transistors for Enumeration of Circulating Tumor Cells. *Lab Chip* **2019**, *19* (4), 618-625.
(36) Adams, T. N.; Jiang, A. Y.; Vyas, P. D.; Flanagan, L. A. J. M. Separation of Neural Stem Cells by Whole Cell Membrane Capacitance Using Dielectrophoresis. *Methods* **2018**, *133*, 91-103.
(37) Chiu, T.-K.; Chao, A.-C.; Chou, W.-P.; Liao, C.-J.; Wang, H.-M.; Chang, J.-H.; Chen, P.-H.; Wu, M.-H. J. S.; Chemical, A. B. Optically-Induced-Dielectrophoresis (ODEP)-Based Cell Manipulation in a Microfluidic System for High-Purity Isolation of Integral Circulating Tumor Cell (CTC) Clusters Based on Their Size Characteristics. *Sensors and Actuators B: Chemical* **2018**, *258*, 1161-1173.
(38) Wu, M.; Chen, K.; Yang, S.; Wang, Z.; Huang, P.-H.; Mai, J.; Li, Z.-Y.; Huang, T. J. J. L. o. a. C. High-Throughput Cell Focusing and Separation via Acoustofluidic Tweezers. *Lab Chip* **2018**, *18* (19), 3003-3010.

Table of Contents artwork